

A Two-step-training Deep Learning Framework for Real-time Computational Imaging without Physics Priors

RUIBO SHANG, KEVIN HOFFER-HAWLIK, AND GEOFFREY P. LUKE*

Thayer School of Engineering, Dartmouth College, 14 Engineering Dr., Hanover, NH 03755, USA

**geoffrey.p.luke@dartmouth.edu*

Abstract: Deep learning (DL) is a powerful tool in computational imaging for many applications. A common strategy is to reconstruct a preliminary image as the input of a neural network to achieve an optimized image. Usually, the preliminary image is acquired with the prior knowledge of the model. One outstanding challenge, however, is that the model is sometimes difficult to acquire with high accuracy. Another main challenge is that the process to reconstruct the preliminary image is time consuming, which cannot achieve real-time imaging. In this work, a two-step-training DL (TST-DL) framework is proposed for real-time computational imaging without prior knowledge of the model. A single fully-connected layer (FCL) is trained to directly learn the model with the raw measurement data as input and the image as output. Then, this pre-trained FCL is fixed and connected with an un-trained deep convolutional network for a second-step training to improve the output image fidelity. This approach has three main advantages. First, no prior knowledge of the model is required since the first-step training is to directly learn the model. Second, real-time imaging can be achieved since the raw measurement data is directly used as the input to the model. Third, it can handle any dimension of the network input and solve the input-output dimension mismatch issues which arise in convolutional neural networks. We demonstrate this framework in the applications of single-pixel imaging and photoacoustic imaging for linear model cases. The results are quantitatively compared with those from other DL frameworks and model-based optimization approaches. Noise robustness and the required size of the training dataset are studied for this framework. We further extend this concept to nonlinear models in the application of image de-autocorrelation by using multiple FCLs in the first-step training. Overall, this TST-DL framework is widely applicable to many computational imaging techniques for real-time image reconstruction without the physics priors.

© 2019 Optical Society of America under the terms of the [OSA Open Access Publishing Agreement](#)

1. Introduction

Computational Imaging is a powerful tool in the applications of image reconstruction. It relaxes the hardware requirements of imaging systems by relying on (typically iterative) computational techniques to recover the lost information, that is, solving an inverse imaging problem computationally [1, 2]. These methods rely on a measured or assumed forward operator of the imaging system to create a mapping from the image to the acquired data. However, the forward operator is often ill-posed due to the imperfect physical measurement, meaning multiple solutions exist for a given measurement. Therefore, additional information about the scene or the object must be incorporated in the computational process for accurate reconstruction.

One of the most common methods in computational imaging is sparsity-based optimization which seeks to reconstruct images from incomplete data or an ill-posed forward operator [3, 4]. This concept is based on the knowledge that most natural images are sparse (i.e., only a few nonzero values exist) when transformed into a specific domain. Researchers have successfully applied sparsity-based optimization in a variety of imaging fields ranging from compressed ultrafast photography [5] to holographic video [6] to biomedical imaging [7]. Although the

sparsity-based optimization has advantages in image reconstruction, the primary drawback to this approach is that it is iterative and time consuming. Depending on the scale and scope of the problem, an image reconstruction task can require minutes to even hours of computation. Therefore, it cannot achieve real-time imaging (data acquisition and image reconstruction are done simultaneously) for many applications. Furthermore, the optimal algorithm-specific parameters in the sparsity-based optimization must be heuristically determined.

Deep learning (DL) [2, 8] is an emerging computational imaging approach dramatically improving the state-of-the-art in real-time image reconstruction [9-14]. Instead of building a specific model and finding the optimal algorithm-specific parameters heuristically (as in sparsity-based optimization approaches), it relies on large amounts of data to automatically learn tasks by using the backpropagation algorithm to find the optimal parameters in each layer of a neural network [8]. It has the benefit of being computationally efficient since most of the computational energy is used during the one-time training process. Compared with sparsity-based optimization approaches which require iterative testing of the regularizer for each image [15], DL approaches utilize the training dataset to find the optimal regularizer for the broad range of images. Therefore, DL is a promising alternative to augment or replace the iterative algorithms used in sparsity-based optimization. Researchers have applied the DL approach in many imaging fields with varying network structures [2]. The U-Net architecture is one of the most successful DL frameworks in the imaging field. Its architecture consists of a contracting path to capture context and a symmetric expanding path for precise localization. Skipped connections between the contracting and expanding path help to preserve features from the input image. A variety of applications in the imaging field have harnessed the original or a modification of the U-Net structure [16-22]. Despite the advantages of these DL approaches in image reconstruction, there are still some limitations. First, a large dataset is usually required to train the network and it must span the space of possible images one would expect to encounter. Second, most of the current DL techniques still require knowledge of the imaging forward model for an initial image guess to feed into the DL networks [14, 20, 23, 24]. However, the forward model in many imaging fields can be difficult to acquire with high accuracy [6, 25, 26] or even nonlinear [14, 27]. Furthermore, the initial reconstruction process will sometimes be computationally intensive, especially when using the iterative reconstruction approaches [28, 29]. Third, most of the DL frameworks are designed for a specific application and not widely applicable in other problems. For instance, mismatches of the size and dimensionality between the measurement data and the reconstructed image are not easily addressed in the U-Net architecture which usually requires the input and output images to have the same size and dimensionality [30]. Although a modified U-Net framework in [21] can deal with the image size mismatch issues, it still requires a 2D image as the input.

Therefore, in this paper, a two-step-training DL (TST-DL) framework is proposed for real-time DL-based computational image reconstruction without prior knowledge of the forward model. The first step trains a single fully-connected layer (FCL) (for linear imaging models) or multiple FCLs (for nonlinear imaging models) to approximate the imaging inverse model with the raw measurement data as input and the ground-truth image as output. The weights of this trained FCL are then fixed and an untrained convolutional neural network (U-Net) is concatenated to the network for a second-step training to effectively impose regularization constraints and improve the reconstruction quality of the results predicted from the first-step training. This versatile DL approach is beneficial because it can be applied to virtually any computational imaging system without the prior knowledge of the imaging model (directly learning the model instead). Furthermore, it can yield results in real time with comparable performance to the iterative algorithms. Moreover, it can handle any dimension of the network input and solve the input-output image size- and dimension- mismatch issues. Finally, by incorporating minor changes to the TST-DL network, image reconstruction with nonlinear imaging models can be performed.

2. Methods

2.1 Regularized optimization

Any imaging model can be described by

$$g = \mathbf{H}f \quad (1)$$

where f is the image to be reconstructed, g is the raw measurement data and \mathbf{H} is the forward operator.

The most straightforward way to reconstruct the image f is to find the inverse of the forward operator \mathbf{H}^{-1} so that $\mathbf{H}^{-1}\mathbf{H} = \mathbf{I}$ where \mathbf{I} is the identity matrix. However, for most of the cases, \mathbf{H}^{-1} is not unique or requires excessive computational power to determine.

An effective alternative to directly computing the inverse of the forward model is to iteratively solve the optimization problem,

$$\hat{f} = \underset{f}{\operatorname{argmin}} \|\mathbf{H}f - g\|_2^2 \quad (2)$$

where $\|\cdot\|_2$ denotes the L_2 norm. However, this pseudo-inverse solution is prone to artifacts and noise due to the ill-posed property of the forward operator \mathbf{H} . Therefore, additional information is needed to converge to the correct solution.

A regularized optimization approach can incorporate additional knowledge about the image by adding a regularization term,

$$\hat{f} = \underset{f}{\operatorname{argmin}} \{\|\mathbf{H}f - g\|_2^2 + \lambda\phi(f)\} \quad (3)$$

where ϕ is the regularization operator and λ is the regularization parameter. $\|\mathbf{H}f - g\|_2^2$ is the fidelity term and $\phi(f)$ is the regularization term. The regularization term is to make a balance with the fidelity term by driving the optimized \hat{f} to match a specific regularization rule. The common regularization domains include L_1 norm, TV norm, wavelet domains and so on. However, finding the optimal regularization rule for a specific image dataset is still a challenging problem [15].

Inspired by the regularized optimization approach, we propose TST-DL framework. The first-step training is to train a FCL to learn an optimal \mathbf{H}^{-1} (assuming \mathbf{H} is a linear operator) given the training datasets (g, f) . Then, this pre-trained FCL is fixed and connected with a U-Net for the second-step training to learn an optimal regularization rule to regularize f towards the optimal solution. We further extend this concept to nonlinear models by using multiple FCLs to learn the optimal nonlinear operator \mathbf{H}^{-1} .

2.2 The TST-DL structure

Our TST-DL framework follows a FCL (or multiple FCLs for nonlinear models) and a U-Net architecture as shown in Fig. (1). The DL framework in step 1 consists of a FCL mapping from the raw measurement data (input) to the image (output) (BatchNorm, reshape and permute layers are used for normalization and reshape purposes). With this FCL, the input measurement data and the output image do not need to have the same size or even the same dimensionality. By training the FCL, the optimal inverse operator will be learned given the training datasets. The DL framework in step 2 follows the U-Net architecture connected to the pre-trained FCL from step 1. The U-Net, which utilizes an encoder-decoder structure with concatenated connections to preserve wide-frequency features, was chosen because of its success in solving image-to-image problems. The mean squared error (MSE) is used as the loss function in the first-step training to find the optimal \mathbf{H}^{-1} that minimizes $\|f - \mathbf{H}^{-1}g\|_2^2$. A customized loss function with a combination of root MSE (RMSE) and difference of structural similarity index (DSSIM) is used for the second-step training. The batch size is chosen to be 50 and each training step runs 100 epochs.

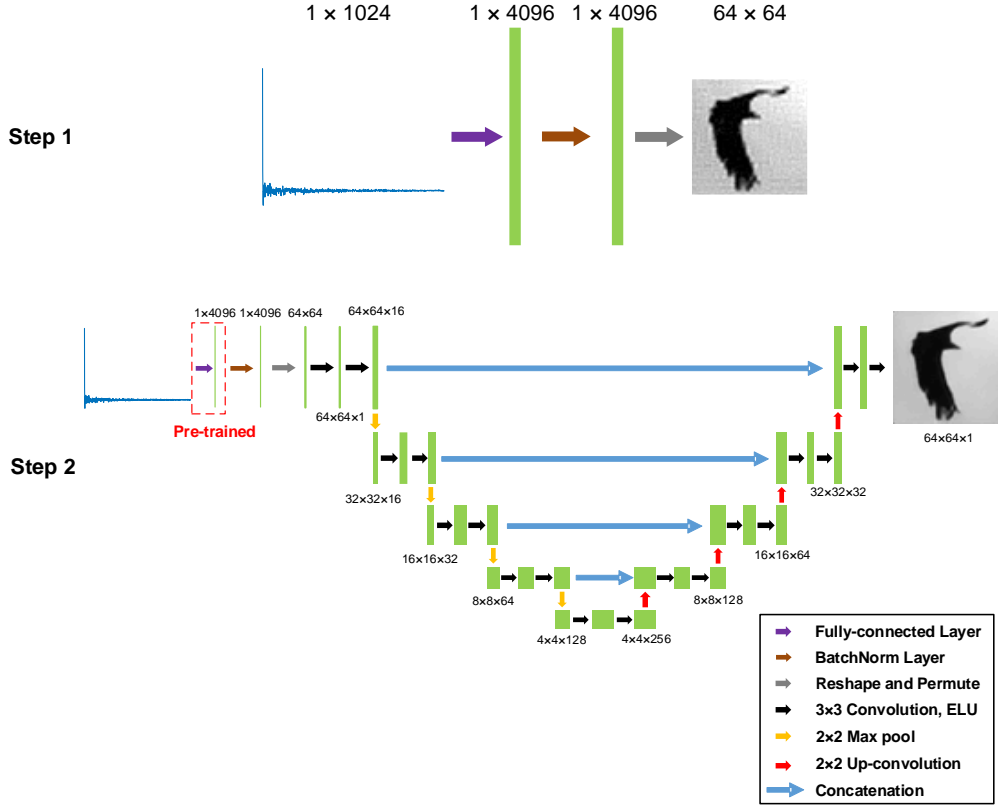


Fig. 1. TST-DL structure. Step 1 is training the FCL and step 2 is training a U-Net with the fixed pre-trained FCL. The input is the raw measurement data that can be any dimension and the output is a 2D image.

3. Data acquisition and results for different imaging models

The data acquisition and results from the prediction of the TST-DL for the single-pixel imaging with Russian-Doll (RD) Hadamard [31] and random Hadamard patterns, photoacoustic (PA) imaging [32-34], and image de-autocorrelation are shown in this section. Quantitative comparisons are made with other DL frameworks (a deep convolutional auto-encoder network (DCAN) [35], one-step-training DL (OST-DL) and U-Net) and the conventional model-based optimization approaches (an iterative L2 norm minimization approach LSQR [28] and a two-step iterative shrinkage/thresholding (TwIST) algorithm [29]). The DCAN was developed in single-pixel imaging to reconstruct the dynamic scenes from the single-pixel camera capture of the compressed signal. DCAN is comprised of two parts, the encoding part to find the optimal binary filters for the measurement and the decoding part for image reconstruction with a fully-connected layer (FCL) and three convolutional layers [35]. For the U-Net approach, an initial guess of the image is reconstructed using $f_{initial} = H^T g$ where H^T denotes the transpose of the forward operator. Then, the initial guess of the image is used as the input of U-Net for further training and prediction. For OST-DL, the FCL is connected with U-Net for a one-step training instead of training each individually. For all the DL approaches, the prediction and the quantitative comparisons were made on the testing dataset instead of the training dataset.

3.1 Single-pixel Imaging with RD Hadamard patterns

In the first case, the RD Hadamard patterns were used in the single-pixel imaging. In RD Hadamard patterns, the measurement order of the Hadamard basis is reordered and optimized according to their significance for general scenes, such that at discretized increments, the complete sampling for different spatial frequencies is obtained [31].

The STL-10 natural image database [36] was used for training the TST-DL framework with 10,000 images as the training dataset, 2,000 images as the validating dataset and another 2,000 images as the testing dataset. In order to meet the dimension requirement of the RD Hadamard patterns, all the images were down-sampled from 96×96 to 64×64 . The full RD Hadamard basis for a 64×64 image has 4,096 RD Hadamard patterns each with a size of 64×64 . Different compression ratios are used here as 4X, 8X, 16X, 32X, 64X and 128X, corresponding to taking the first 1/4, 1/8, 1/16, 1/32, 1/64, and 1/128 of RD Hadamard patterns, respectively. For instance, for 4X compression, the first 1,024 RD Hadamard patterns are used. The 1D raw measurement data was acquired by multiplying each individual image with the RD Hadamard patterns at each compression ratio. Therefore, the 1D raw measurement data has a size of $1,024 \times 1$, 512×1 , 256×1 , 128×1 , 64×1 and 32×1 for the corresponding compression ratios.

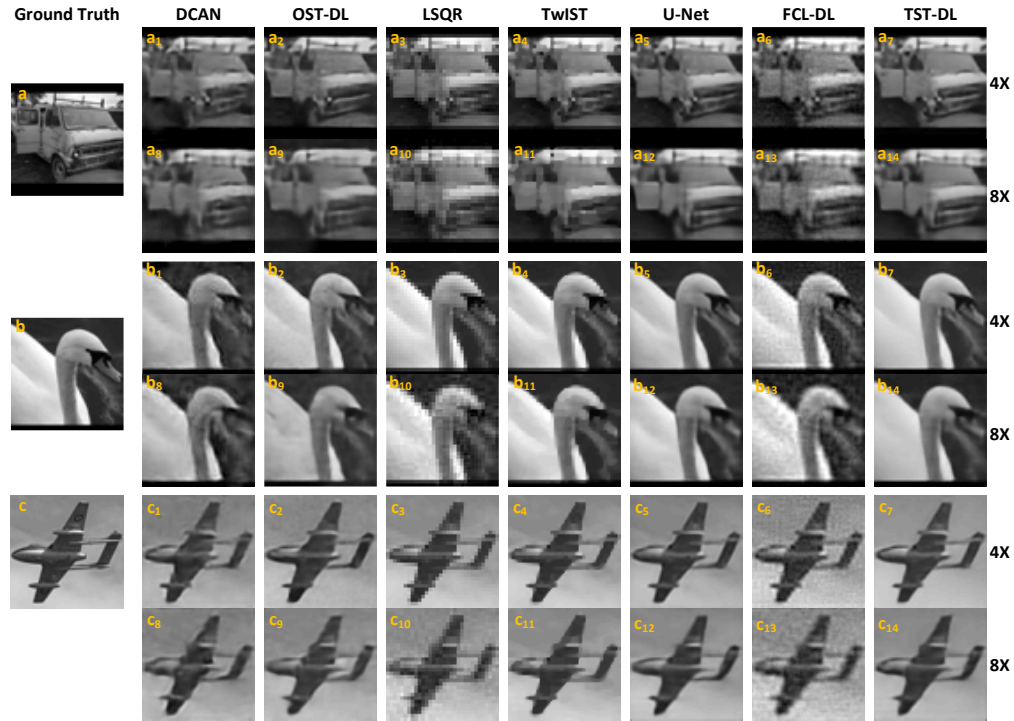


Fig. 2. Three representative reconstructed images in the testing dataset from DCAN, OST-DL, LSQR, TwIST, U-Net, FCL-DL and TST-DL at 4X and 8X compression ratios and their ground truth images. (a) The ground truth image of a van; (a₁-a₇) The reconstructed van images from all the approaches respectively at the 4X compression ratio; (a₈-a₁₄) The reconstructed van images from all the approaches respectively at the 8X compression ratio; (b) The ground truth image of a goose; (b₁-b₇) The reconstructed goose images from all the approaches respectively at the 4X compression ratio; (b₈-b₁₄) The reconstructed goose images from all the approaches respectively at the 8X compression ratio; (c) The ground truth image of an aircraft; (c₁-c₇) The reconstructed aircraft images from all the approaches respectively at the 4X compression ratio; (c₈-c₁₄) The reconstructed aircraft images from all the approaches respectively at the 8X compression ratio.

Table 1. Averaged RMSE and SSIM of the reconstructed images in the testing dataset at 4X and 8X compression ratios for different reconstruction approaches.

| Compression Ratio | | DCAN | OST-DL | LSQR | TwIST | U-Net | FCL-DL | TST-DL |
|-------------------|------|-------|--------|-------|-------|-------|--------|--------|
| 4X | RMSE | 0.074 | 0.059 | 0.060 | 0.051 | 0.050 | 0.051 | 0.051 |
| | SSIM | 0.768 | 0.803 | 0.830 | 0.865 | 0.865 | 0.816 | 0.833 |
| 8X | RMSE | 0.081 | 0.079 | 0.072 | 0.061 | 0.059 | 0.063 | 0.063 |
| | SSIM | 0.701 | 0.700 | 0.705 | 0.780 | 0.787 | 0.727 | 0.762 |

The reconstructed images at 4X and 8X compression ratios from multiple reconstruction approaches are shown in Fig. (2). The images from the TST-DL are shown in the last column and compared with the other three DL frameworks (DCAN, OST-DL and U-Net) and the conventional model-based optimization approaches (LSQR and TwIST). The intermediate results from the first-step training using the FCL in TST-DL are also shown as FCL-DL. Table 1 shows the averaged RMSE and structural similarity index (SSIM) [37] of the reconstructed images in the testing dataset at 4X and 8X compression ratios from all the reconstruction approaches (For LSQR and TwIST, 500 images in the testing dataset were reconstructed and used to calculate the averaged RMSE and SSIM instead of the full testing dataset in the interest of time). From Fig. 2 and Table 1, we can see that the results from the conventional model-based optimization approaches (LSQR and TwIST) are comparable to the DL approaches. Moreover, both LSQR and TwIST approaches require accurate knowledge of the forward operator for image optimization. In addition, reconstruction from LSQR and TwIST require thousands of iterations, which cannot achieve real-time imaging. Therefore, for real-time imaging with the forward operator in low accuracy or even not available, LSQR and TwIST are not the best options.

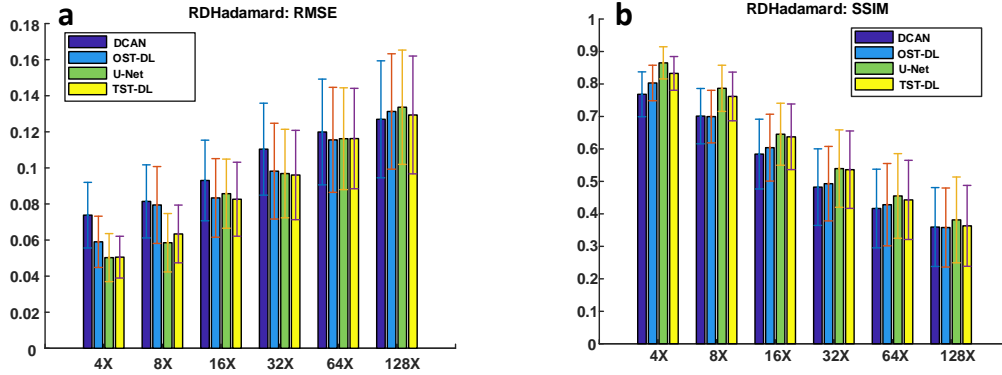


Fig. 3. Quantitative comparison in terms of RMSE and SSIM; (a) RMSE for DCAN, OST-DL, U-Net and TST-DL in all compression ratios with RD Hadamard patterns; (b) SSIM for DCAN, OST-DL, U-Net and TST-DL in all compression ratios with RD Hadamard patterns.

For further quantitative comparison with the other three DL frameworks, the mean and the standard deviation of the RMSE and SSIM are calculated through the 2,000 testing images at all the compression ratios as shown in Fig. 3. We can see that for most of the cases, the U-Net approach is the best. This makes sense since the initial guess of the input images in U-Net needs the physics priors of the forward operator. It is obvious that the more you know about the model, the better reconstruction results you will get. For TST-DL, even though the physics priors of the model are unknown, the results are almost equivalent to those from U-Net and outperform those from DCAN and OST-DL. Therefore, for approaches without the physics priors of the model, TST-DL is the best in terms of RMSE and SSIM for all compression ratios.

3.2 Single-pixel Imaging with random Hadamard patterns

In the second case, random Hadamard patterns were used in the single-pixel imaging to see how TST-DL performs in a more challenging case since the reconstruction is more difficult than that from the RD Hadamard patterns [38]. The random Hadamard patterns were generated in Matlab by randomly permuting a full basis of 4,096 64×64 pixel patterns. The same training, validating and testing dataset were used here as in the RD Hadamard case. For random Hadamard patterns, we only reconstruct the images at 4X and 8X compression ratios.

Fig. (4) shows representative results at the 4X compression ratio from DCAN, OST-DL, U-Net, TST-DL, and the ground truth images. Visually, it can be seen that the TST-DL performs better than the other 3 DL frameworks. The fine details of the images can be reconstructed from TST-DL while they are only partially reconstructed or totally missed in other DL frameworks. For instance, in Fig. c_1 - c_5 , the tire of the van can be fully reconstructed in TST-DL while it is partially reconstructed or totally missed in DCAN, OST-DL and U-Net.

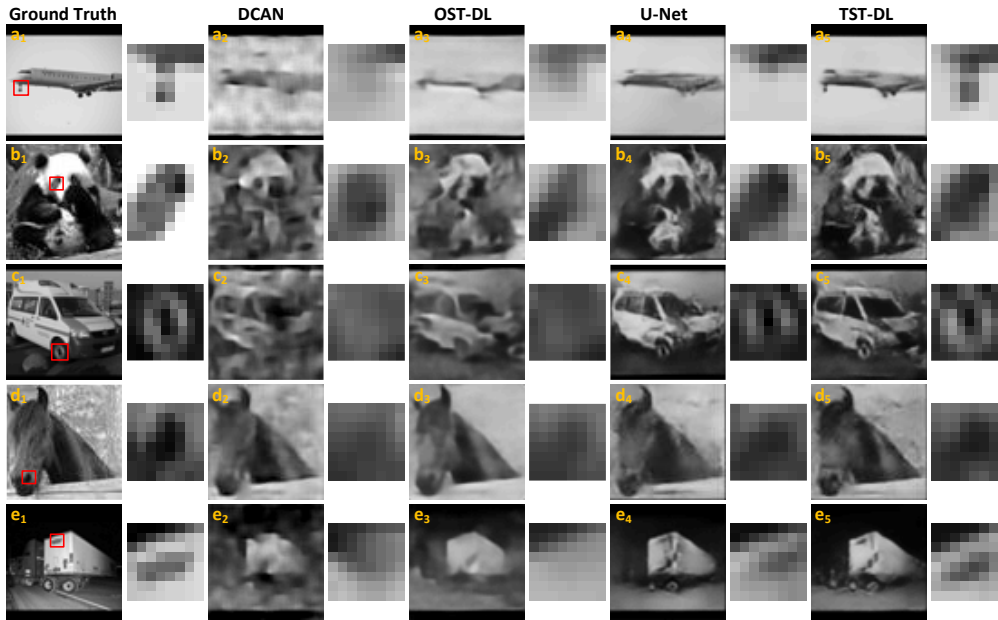


Fig. 4. Five representative reconstructed images in the testing dataset from DCAN, OST-DL, U-Net, TST-DL and some detailed features with the random Hadamard patterns at the 4X compression ratio and the ground truth images. (a_1 - a_5) The ground-truth image of an aircraft and the reconstructed images from DCAN, OST-DL, U-Net and TST-DL with the detailed feature of the undercarriage; (b_1 - b_5) The ground-truth image of a panda and the reconstructed images from DCAN, OST-DL, U-Net and TST-DL with the detailed feature of the eye; (c_1 - c_5) The ground-truth image of a van and the reconstructed images from DCAN, OST-DL, U-Net and TST-DL with the detailed feature of the wheel; (d_1 - d_5) The ground-truth image of a horse and the reconstructed images from DCAN, OST-DL, U-Net and TST-DL with the detailed feature of the nose; (e_1 - e_5) The ground-truth image of a truck and the reconstructed images from DCAN, OST-DL, U-Net and TST-DL with the detailed feature of the label.

To quantitatively compare the results, the mean and the standard deviation of the RMSE and SSIM in the testing dataset were calculated for all the 4 DL frameworks as shown in Fig. (5) at 4X and 8X compression ratios. Figure 5 shows that TST-DL performs better than the other 3 DL frameworks with lower RMSE and higher SSIM. Interestingly, it is even better than the U-Net approach which requires the knowledge of the forward model for an initial guess of the image. The reason is that the random Hadamard matrix is less coherent than RD Hadamard matrix so that the initial guess of the image does not include many features about the image.

Thus, we expect that as the information-preserving ability of the forward model degrades, the TST-DL approach will further improve.

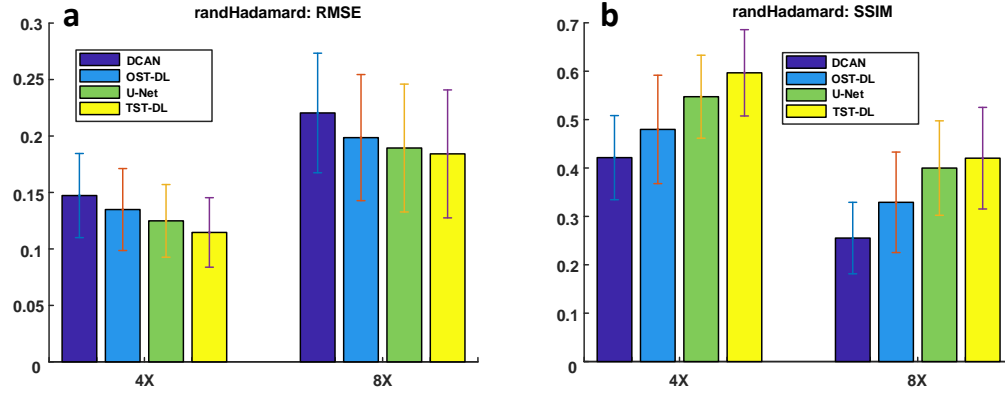


Fig. 5. Quantitative comparison in terms of RMSE and SSIM; (a) RMSE for DCAN, OST-DL, U-Net and TST-DL with the random Hadamard patterns at 4X and 8X compression ratios; (b) SSIM for DCAN, OST-DL, U-Net and TST-DL with the random Hadamard patterns at 4X and 8X compression ratios.

3.3 PA imaging with a linear array ultrasound transducer

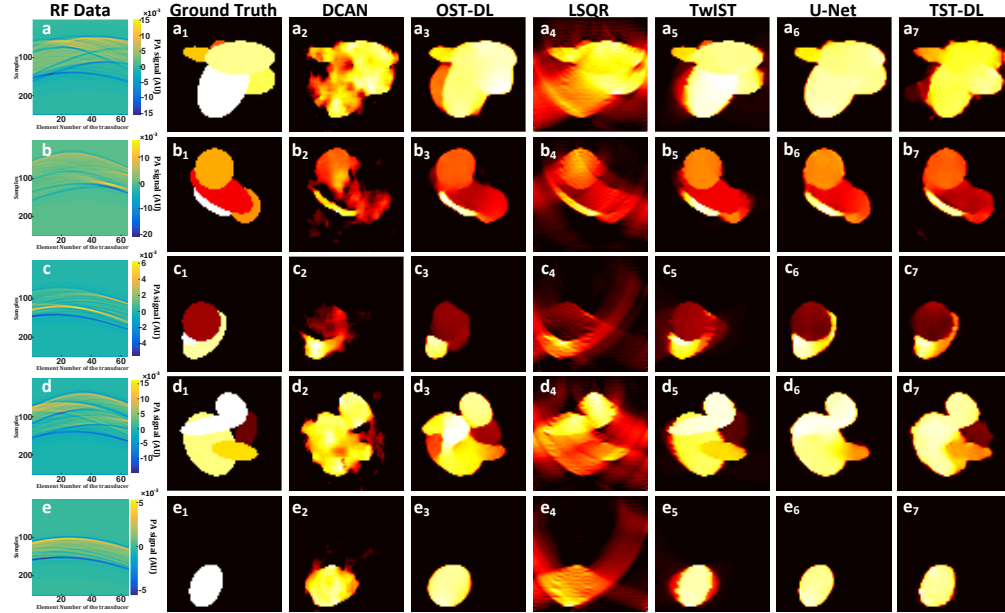


Fig. 6. Five representative reconstructed images (a-e) in the testing dataset from DCAN, OST-DL, LSQR, TwIST, U-Net and TST-DL together with the corresponding RF data and the ground truth images.

PA imaging with a linear array ultrasound transducer is used as the third case to prove that TST-DL can be applied to a wide range of imaging modalities. 9,000 PA objects were simulated as the ground truth images with random number of oval objects randomly located in the FOV similar to the blood vessel cross-sections one would encounter in biomedical PA imaging. These objects have random intensities ranging from 0 to 1. The size of each image is 64×64 . The k-Wave toolbox [39] was used to simulate the corresponding RF data with a simulated 64-element linear array ultrasound transducer (0.15mm pitch size) oriented horizontally on top of

the object to be imaged. A sampling frequency of 22 MHz and a center frequency of 6 MHz with a bandwidth of 4.8 MHz was used. After the simulation, we vectorized the 2D RF data as the input of DCAN, OST-DL and TST-DL. We used 5,000 RF datasets and the corresponding ground truth images as the training dataset, 2,000 RF data and the corresponding ground truth images as the validating dataset, and 2,000 RF data and the corresponding ground truth images as the testing dataset. For the U-Net, the back-projection images are used as the input images and the corresponding ground truth images as the output images. The conventional model-based iterative optimization approaches (LSQR and TwIST) are also included for comparison.

Fig. (6) shows the reconstructed results from DCAN, OST-DL, LSQR, TwIST, U-Net and TST-DL together with the corresponding input RF data and the ground truth images. The DCAN and LSQR approaches have the bad results for all the 5 reconstructed images. Specifically, the LSQR approach cannot remove the image artifacts coming from the finite aperture of the linear array ultrasound transducer. The OST-DL, TwIST, U-Net and TST-DL have the reasonably good reconstructions for all the 5 images although tiny image mismatch happens. To further quantitatively compare the results, the mean and standard deviation of the RMSE and SSIM for all the reconstructed images in the testing dataset in all the approaches were calculated and shown in Fig. (7).

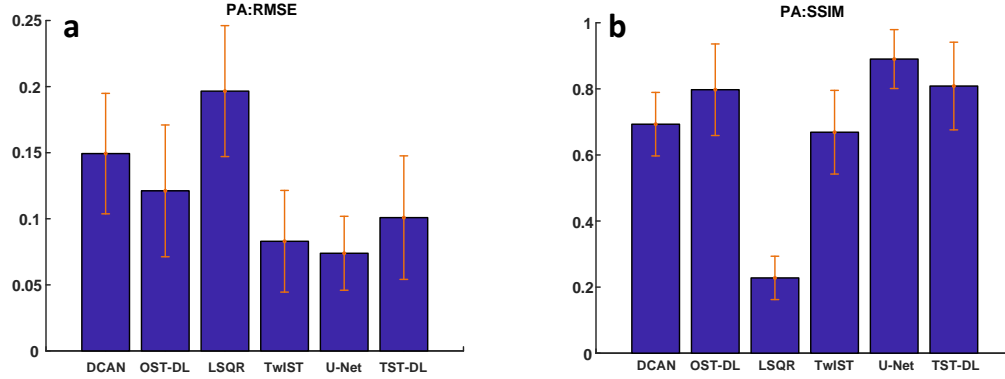


Fig. 7. Quantitative comparison in terms of RMSE and SSIM; (a) RMSE for DCAN, OST-DL, LSQR, TwIST, U-Net and TST-DL; (b) SSIM for DCAN, OST-DL, LSQR, TwIST, U-Net and TST-DL.

Overall, the U-Net demonstrates the best performance compared with other approaches. The result is reasonable since the forward operator is known and used for back-projection reconstruction as the input image of U-Net. The LSQR approach has the worst results because of its failure to remove artifacts. For all the approaches without the physics prior of the forward operator, TST-DL performs the best with a lower RMSE and a higher SSIM. Therefore, for real-time imaging without physics priors, TST-DL still performs the best.

3.4 Noise robustness

Since noise exists in the measurement data for most of the real cases, different levels of white Gaussian noise (-10dB, -5dB, 0dB and 5dB SNR levels) were added to the 1D measured signals in single-pixel imaging with RD Hadamard patterns at the 4X compression ratio to test the robustness of the methods to noise. The mean and standard deviation of the RMSE and SSIM for all the reconstructed images in the testing dataset at each noise level are calculated to quantitatively compare the performance as shown in Fig. 8(a). It shows that with the increase of the noise level (decrease of the SNR), the reconstruction performance is dropping with the increase of the RMSE and decrease of the SSIM. However, the results still remain at a reasonable level with the RMSE lower than 0.1 and SSIM larger than 0.55.

Fig. 8(c-f) show the reconstructed images at -10dB, -5dB, 0dB and 5dB noise level with the same ground truth image in Fig. 8(b). Although the reconstructed images become more and

more blurred with the increase of the noise, the general shape and even some of the details (the top of the tower in the zoom-in figures) can still be well reconstructed at the -5dB, 0dB and 5dB SNR levels. Given the SNR levels -10dB, -5dB, 0dB and 5dB are extremely high levels of noise (for 0dB, the noise level is the same as the signal level), we can conclude that TST-DL is robust to noise.

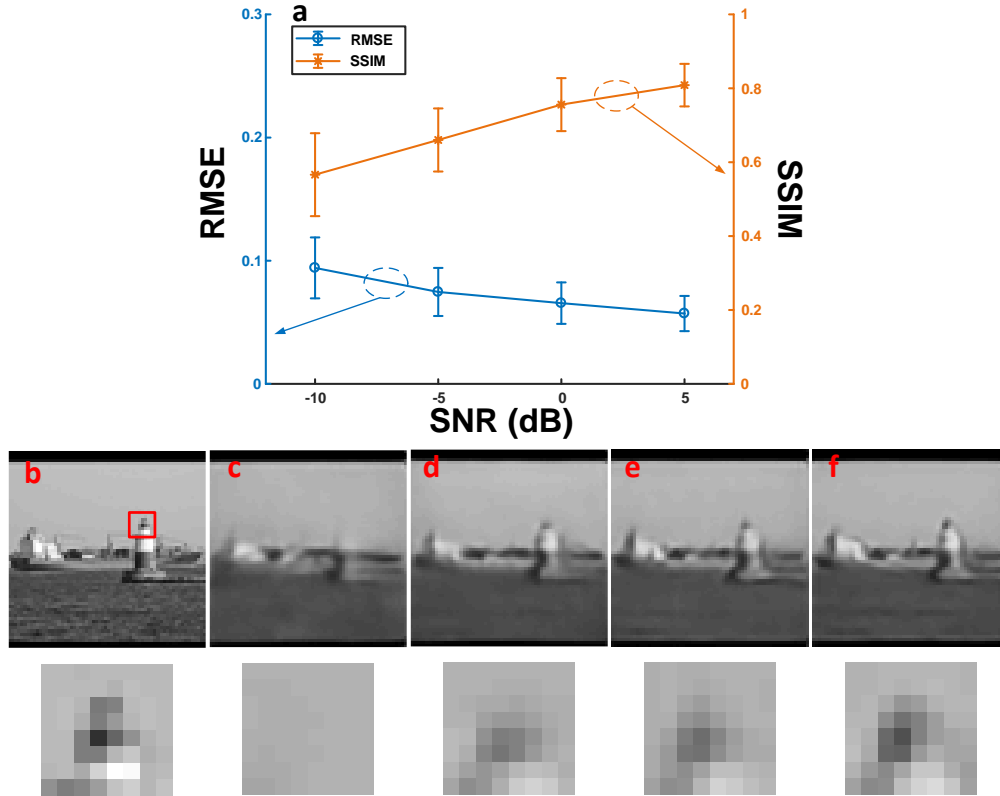


Fig. 8 Noise robustness test; (a) RMSE and SSIM of the TST-DL results at the -10dB, -5dB, 0dB and 5dB SNR levels; (b) The ground truth of an image in the testing dataset; (c) The TST-DL prediction of the image in (b) at the -10dB SNR level; (d) The TST-DL prediction of the image in (b) at the -5dB SNR level; (e) The TST-DL prediction of the image in (b) at the 0dB SNR level; (f) The TST-DL prediction of the image in (b) at the 5dB SNR level.

3.5 Reducing the size of the training dataset

Since large training dataset is not always available for real cases, the size of the training dataset is also a key factor in DL frameworks. Therefore, we tested the impact of the size of the training dataset in the TST-DL to find a reasonable size of the training dataset while still maintaining good reconstruction results.

Fig. 9(a) shows the TST-DL performance of the prediction in the same testing dataset with the RD Hadamard patterns at the 4X compression ratio in terms of RMSE and SSIM with 625, 1,250, 2,500, 5,000 and 10,000 training images. The results shows that with the decrease of the number of training samples, the TST-DL performance drops but still remains reasonably good at the case of 2,500 training images. Fig. 9(c-g) show the reconstruction results of the same image in the testing dataset with 625, 1,250, 2,500, 5,000 and 10,000 training images respectively together with the ground truth image in Fig. 9(b). The image becomes clearer and the detail is better reconstructed with the increase of the number of training samples. Qualitatively, the case of 2,500 training images has a reasonably good reconstruction result,

which is consistent with the quantitative results in Fig. 9(a). Overall, with these results, it can be proved that TST-DL can still perform well with a small training dataset which means that it can be applicable to many real image reconstruction cases where a large training dataset is not available.

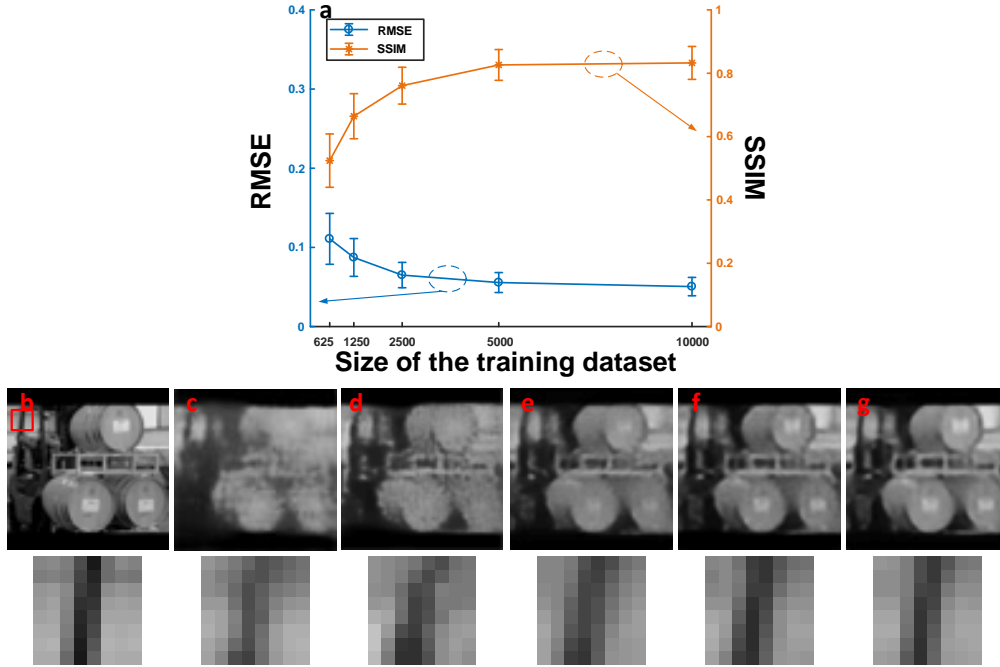


Fig. 9. Reducing the size of the training dataset; (a) The RMSE and SSIM of the TST-DL results with 625, 1,250, 2,500, 5,000 and 10,000 training images; (b) The ground truth of the oil-tank image in the testing dataset and the detailed feature in the red square; (c) The TST-DL prediction of the image and the detailed feature in (b) with 625 training images; (d) The TST-DL prediction of the image and the detailed feature in (b) with 1,250 training images; (e) The TST-DL prediction of the image and the detailed feature in (b) with 2,500 training images; (f) The TST-DL prediction of the image and the detailed feature in (b) with 5,000 training images; (g) The TST-DL prediction of the image and the detailed feature in (b) with 10,000 training images.

3.6 Image de-autocorrelation

For all the above reconstruction cases, the imaging model is linear such that the forward operator can be described as a 2D matrix and the forward model and its inverse can both be described as matrix multiplication. TST-DL has proven effective at handling these imaging models since the FCL in the first-step training exactly corresponds to matrix multiplication. Here, we extend the utility of TST-DL to handle nonlinear imaging models which cannot be described as matrix multiplication. Image autocorrelation is a nonlinear model such that the inverse process, image de-autocorrelation is also a nonlinear process. One of the important applications of image de-autocorrelation is to reconstruct the image through scattering medium [27] which is to solve a phase-retrieval problem from the Fourier magnitude measurement [40, 41]. Therefore, we applied TST-DL to the image de-autocorrelation problem as a test case for the nonlinear model. The MNIST database [42] handwriting numbers were used as the ground truth images. The raw images in MNIST were resized from 28×28 to 64×64 pixels. 10,000 images from the training dataset in MNIST were used as the training dataset, 2,000 images from the testing dataset in MNIST were used as the validating dataset and another 2,000 images from the testing dataset in MNIST were used as the testing dataset. Then, the image autocorrelation was applied to each of the images. The autocorrelated images were used as the input of TST-DL and their corresponding ground truth images were used as the output of the

network to achieve image de-autocorrelation. In order to handle nonlinear models, a slight modification is made to TST-DL by using 4 FCLs connected in series instead of a single FCL in the first-step training. More FCLs with a nonlinear activation function will add more nonlinearity to the DL networks to handle the nonlinear imaging problems.

Previously [27], the image de-autocorrelation was achieved through phase-retrieval algorithms. Therefore, we compare the results with those from the Gerchberg-Saxton phase-retrieval algorithm [40]. Fig. 10 shows the reconstruction results with images in Fig. 10 (a-j) to be the autocorrelation images, Fig. 10(a₁-j₁) to be the ground truth images, Fig. 10(a₂-j₂) to be the reconstructed images from the phase retrieval algorithm and Fig. 10(a₃-j₃) to be the reconstructed images from TST-DL. From the results, we can find that the phase retrieval algorithm sometimes fails to work because of twinned image artifacts in the reconstructed images while TST-DL is much more robust. For further quantitative comparison, the RMSE and SSIM were calculated. The RMSE for all the reconstructed images in the testing dataset is 0.137 for TST-DL and 0.155 for the phase retrieval. The corresponding SSIM is 0.815 for TST-DL and 0.727 for the phase retrieval. Therefore, TST-DL has a more stable reconstruction than the phase retrieval algorithm and performs better in terms of RMSE and SSIM. It also means that TST-DL is able to handle nonlinear inverse imaging problems with a slight modification.

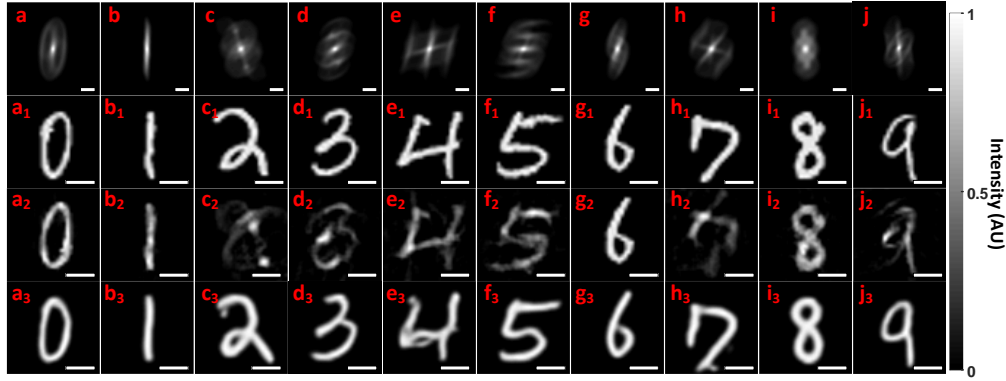


Fig. 10. Image de-autocorrelation results of ten representative images in the testing dataset from TST-DL; (a-j) Autocorrelated images; (a₁-j₁) Ground truth images; (a₂-j₂) Reconstructed images from the phase retrieval algorithm; (a₃-j₃) Reconstructed images from TST-DL. The scale bar denotes 20 pixels.

4. Experimental results

4.1 Training dataset collection

In order to demonstrate that the TST-DL framework can be applied to experimental data, we have applied the method to our experiment PA imaging system. The impulse responses in PA imaging were collected as the training dataset in the experiment using previously published methods [7]. A 0.2-mm diameter graphite rod was immersed into water with its cross section to be used as the point source for the impulse response measurements. Then, 0.035 mg/ml of titanium dioxide was added into water as scatterers to mimic the scattering effects in the real biological tissues. 7-ns laser pulses at a 10-Hz repetition rate ($\lambda = 770$ nm) from an Nd:YAG 2nd harmonic pumped optical parametric oscillator (OPO) laser system (Phocus Mobile HE, Opotek Inc.) was used to illuminate the graphite rod. The PA signal from the optical absorption in the graphite was acquired simultaneously by the 128 elements of a linear array ultrasound transducer (L11-4V, Verasonics, pitch size 0.3mm) connected to a Verasonics Vantage 256 ultrasound imaging system (sampling frequency 22.7MHz) [7]. A 2D stepper motor was used to move the graphite rod in lateral and axial directions to measure the impulse responses at different locations in the FOV. For the purpose of shortening experimental time as mentioned in [7], only the RF dataset of the impulse response from 64×64 points in the FOV were collected

with only 64 elements of the ultrasound transducer. Therefore, a total of 4,096 impulse responses were collected. Then, these impulse responses were reordered in a random order and vectorized individually, and the first 3,200 of them and their corresponding spatial location image were taken as the training dataset. Fig. 11 (a-c) show the three representative spatial location images as the output of the TST-DL network for training and Fig. 11 (d-f) show their corresponding impulse responses as the input of the TST-DL network for training after vectorization. The noise in the RF data in Fig. 11 (d-f) is from the extra reflection in the medium.

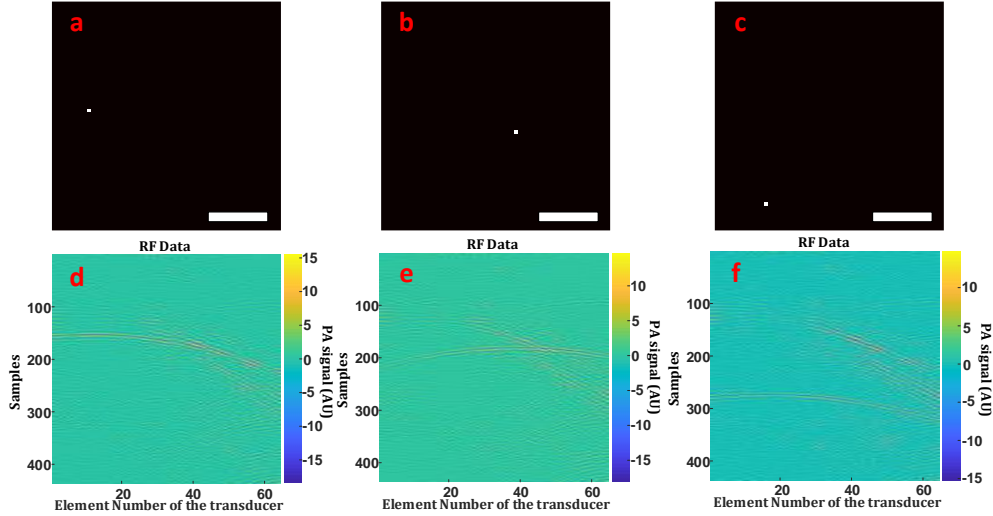


Fig. 11. Representative images in the training dataset; (a-c) Spatial location images as the output of the TST-DL network for training; (d-f) RF data of the impulse responses as the input of the TST-DL network for training after vectorization. The scale bar denotes 5mm.

4.2 TST-DL prediction for the tissue-mimicking phantom

The PA signal from a polyacrylamide tissue-mimicking phantom [43] as mentioned in Sec. 4.2 and Fig. 6 (a-c) in [7] was used as the testing dataset for TST-DL prediction. This tissue-mimicking phantom contains two 0.2-mm diameter graphite rods and dissolved 7 mg of the titanium dioxide for a concentration of 0.035mg/ml to mimic the same scattering effect as in the impulse response measurement experiment. Since the back projection and TwIST approaches perform well in reconstructing point objects, we used their results as an indication of the ground truth (or close to the ground truth since errors occur sometimes). And since TST-DL outperforms the other non-physics-priors DL frameworks in all the simulations, we only compare the TST-DL with TwIST (an iterative reconstruction approach) and the back projection (a non-iterative reconstruction approach). In addition, since the RF data of the tissue-mimicking phantom (the testing dataset) has higher level of noise than that from the impulse response RF data (the training dataset) because of the medium difference, the TST-DL prediction will have some noise on the background. Therefore, a threshold of 0.5 was applied to the TST-DL predicted images after normalization as well as to the back projection and TwIST results (any pixel value less than or equal to 0.5 will be set to 0).

Fig. 12 shows the experimental reconstructed results on the tissue-mimicking phantom at 4 scanning locations. Fig. 12 (a-d) show the RF data at the 4 scanning locations. Fig. 12 (a₁-d₁) show the reconstructed images from the back projection approach as a non-iterative reconstruction approach. Fig. 12 (a₂-d₂) show the reconstructed images from TwIST as an iterative reconstruction approach. Fig. 12 (a₃-d₃) show the reconstructed images from TST-DL. Ideally, there should be only two points in the reconstructed images since the diameter of the two graphite rods in the phantom is smaller than the resolution of the reconstructed images.

The extra non-zero signal in the reconstructed PA images might be from the extra reflection in the phantom. Compared with the ground truth images from the back projection and TwIST approaches, TST-DL predicts the points at the correct location with high precision. Especially for the reconstructed images from the RF data in Fig. 12(d₁), one scatterer is missing in both back projection and TwIST results in Fig. 12 (d₂) and Fig. 12 (d₃) while it is reconstructed in TST-DL in Fig. 12 (d₄). Therefore, TST-DL can be proved to be a reliable image reconstruction tool in real experiments.

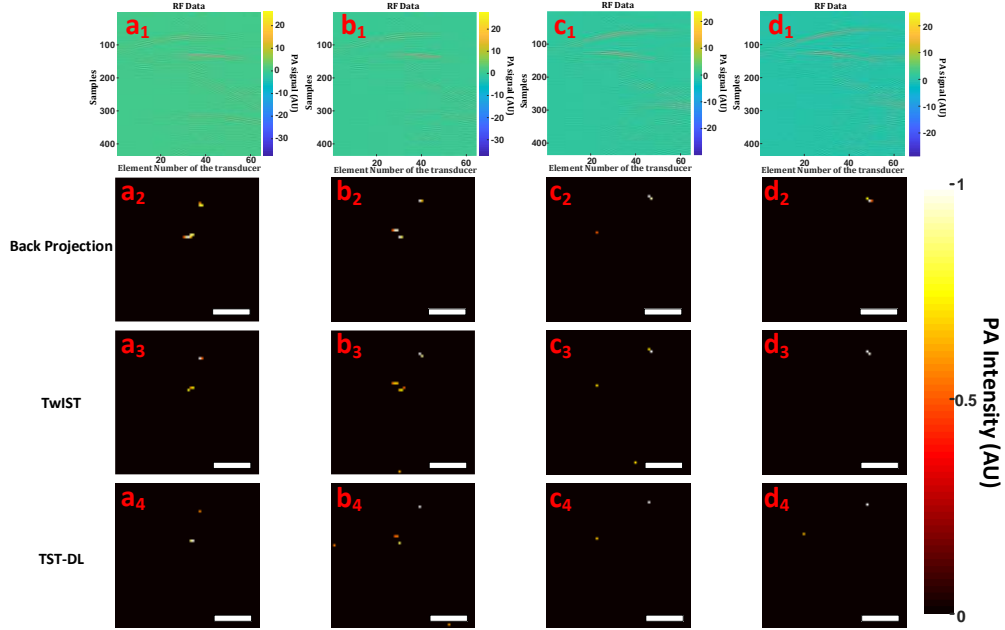


Fig. 12. Experimental results on tissue-mimicking phantom reconstruction. (a₁-d₁) The RF data at 4 scanning locations; (a₂-d₂) Reconstructed images from the back projection approach; (a₃-d₃) Reconstructed images from TwIST; (a₄-d₄) Reconstructed images from TST-DL. The scale bar denotes 5mm.

5. Conclusions and discussion

In conclusion, a TST-DL framework is proposed for real-time image reconstruction without prior knowledge about the model and handling the input-output image size and dimension mismatch issues. The FCL in the first-step training is to directly learn the inverse of the forward operator given the training data. Then, the pre-trained FCL is fixed and connected with a U-Net for a second-step training to find the optimal regularizer to regularize the image for optimization. Four simulations with different imaging models (single-pixel imaging with RD Hadamard matrix, single-pixel imaging with random Hadamard matrix, PA imaging and image de-autocorrelation) were conducted to verify the effectiveness of the proposed TST-DL with quantitative comparison with other DL frameworks and the iterative model-based optimization approaches. The averaged time to predict an image from the testing dataset in TST-DL is ≤ 1 ms in the simulations. An experiment was conducted in PA imaging with training $\sim 80\%$ of the impulse responses data and testing on the tissue-mimicking phantom data. The results show the TST-DL outperforms the other DL frameworks without physics priors and is comparable to (sometime even better than) the DL framework and iterative optimization approaches that know the forward operator.

Although the TST-DL framework shows superior performance in these studies, there are still some trade-offs in the framework. A relatively large number of the training data is needed to optimize the parameters since the FCL is used to directly learn the model in the first step of

TST-DL and it has a large number of parameters to train. Therefore, obtaining enough training samples in the real experiment for training is still a challenging issue although the problem occurs in most DL frameworks. In addition, training a large number of parameters also means taking up a large computer memory such that a powerful computer (such as a workstation) is a requirement while the commonly used DL frameworks with convolutional neural networks is applicable in a normal desktop with lower power requirement. Besides, although it is proved that TST-DL can also reconstruct the images in nonlinear imaging models, further exploration is still needed in determining the optimal number of FCLs to use and the choose of the nonlinear activation functions in each FCL.

6. Funding and disclosures

6.1 Funding

This work was supported by a Faculty Grant from the Neukom Institute for Computational Science at Dartmouth College.

6.2 Disclosures

The authors declare no conflicts of interest.

References

1. J. N. Mait, G. W. Euliss, and R. A. Athale, "Computational imaging," *Advances in Optics and Photonics* **10**, 409-483 (2018).
2. G. Barbastathis, A. Ozcan, and G. Situ, "On the use of deep learning for computational imaging," *Optica* **6**, 921-943 (2019).
3. E. Candes, and J. Romberg, "Sparsity and incoherence in compressive sampling," *Inverse problems* **23**, 969 (2007).
4. E. J. Candès, and M. B. Wakin, "An introduction to compressive sampling [a sensing/sampling paradigm that goes against the common knowledge in data acquisition]," *IEEE signal processing magazine* **25**, 21-30 (2008).
5. L. Gao, J. Liang, C. Li, and L. V. Wang, "Single-shot compressed ultrafast photography at one hundred billion frames per second," *Nature* **516**, 74 (2014).
6. Z. Wang, L. Spinoulas, K. He, L. Tian, O. Cossairt, A. K. Katsaggelos, and H. Chen, "Compressive holographic video," *Optics express* **25**, 250-262 (2017).
7. R. Shang, R. Archibald, A. Gelb, and G. P. Luke, "Computational photoacoustic imaging with sparsity-based optimization of the initial pressure distribution," in *Photons Plus Ultrasound: Imaging and Sensing 2018*(International Society for Optics and Photonics2018), p. 104944Q.
8. Y. LeCun, Y. Bengio, and G. Hinton, "Deep learning," *nature* **521**, 436 (2015).
9. Y. Rivenson, Z. Göröcs, H. Günaydin, Y. Zhang, H. Wang, and A. Ozcan, "Deep learning microscopy," *Optica* **4**, 1437-1443 (2017).
10. Y. Rivenson, Y. Zhang, H. Günaydin, D. Teng, and A. Ozcan, "Phase recovery and holographic image reconstruction using deep learning in neural networks," *Light: Science & Applications* **7**, 17141 (2018).
11. Y. Li, Y. Xue, and L. Tian, "Deep speckle correlation: a deep learning approach toward scalable imaging through scattering media," *Optica* **5**, 1181-1190 (2018).
12. Y. Xue, S. Cheng, Y. Li, and L. Tian, "Reliable deep-learning-based phase imaging with uncertainty quantification," *Optica* **6**, 618-629 (2019).
13. A. Sinha, J. Lee, S. Li, and G. Barbastathis, "Lensless computational imaging through deep learning," *Optica* **4**, 1117-1125 (2017).
14. A. Goy, K. Arthur, S. Li, and G. Barbastathis, "Low photon count phase retrieval using deep learning," *Physical review letters* **121**, 243902 (2018).
15. J. Liu, Q. He, and J. Luo, "A compressed sensing strategy for synthetic transmit aperture ultrasound imaging," *IEEE transactions on medical imaging* **36**, 878-891 (2016).
16. W. Chen, Y. Zhang, J. He, Y. Qiao, Y. Chen, H. Shi, E. X. Wu, and X. Tang, "Prostate segmentation using 2D bridged U-net," in *2019 International Joint Conference on Neural Networks (IJCNN)*(IEEE2019), pp. 1-7.
17. S. Shah, P. Ghosh, L. S. Davis, and T. Goldstein, "Stacked U-Nets: a no-frills approach to natural image segmentation," *arXiv preprint arXiv:1804.10343* (2018).
18. J. Chen, L. Yang, Y. Zhang, M. Alber, and D. Z. Chen, "Combining fully convolutional and recurrent neural networks for 3d biomedical image segmentation," in *Advances in neural information processing systems*(2016), pp. 3036-3044.
19. T. Sun, Z. Chen, W. Yang, and Y. Wang, "Stacked U-Nets With Multi-Output for Road Extraction," in *CVPR Workshops*(2018), pp. 202-206.
20. S. Antholzer, M. Haltmeier, and J. Schwab, "Deep learning for photoacoustic tomography from sparse data," *Inverse problems in science and engineering* **27**, 987-1005 (2019).

21. D. Waibel, J. Gröhl, F. Isensee, T. Kirchner, K. Maier-Hein, and L. Maier-Hein, "Reconstruction of initial pressure from limited view photoacoustic images using deep learning," in *Photons Plus Ultrasound: Imaging and Sensing 2018*(International Society for Optics and Photonics2018), p. 104942S.
22. G. Zhang, T. Guan, Z. Shen, X. Wang, T. Hu, D. Wang, Y. He, and N. Xie, "Fast phase retrieval in off-axis digital holographic microscopy through deep learning," *Optics express* **26**, 19388-19405 (2018).
23. J. Schwab, S. Antholzer, R. Nuster, G. Paltauf, and M. Haltmeier, "Deep Learning of truncated singular values for limited view photoacoustic tomography," in *Photons Plus Ultrasound: Imaging and Sensing 2019*(International Society for Optics and Photonics2019), p. 1087836.
24. S. Guan, A. Khan, S. Sikdar, and P. Chitnis, "Fully Dense UNet for 2D sparse photoacoustic tomography artifact removal," *IEEE journal of biomedical and health informatics* (2019).
25. S. Popoff, G. Lerosey, R. Carminati, M. Fink, A. Boccara, and S. Gigan, "Measuring the transmission matrix in optics: an approach to the study and control of light propagation in disordered media," *Physical review letters* **104**, 100601 (2010).
26. M. Kim, W. Choi, Y. Choi, C. Yoon, and W. Choi, "Transmission matrix of a scattering medium and its applications in biophotonics," *Optics express* **23**, 12648-12668 (2015).
27. O. Katz, P. Heidmann, M. Fink, and S. Gigan, "Non-invasive single-shot imaging through scattering layers and around corners via speckle correlations," *Nature photonics* **8**, 784 (2014).
28. C. C. Paige, and M. A. Saunders, "LSQR: An algorithm for sparse linear equations and sparse least squares," *ACM Transactions on Mathematical Software (TOMS)* **8**, 43-71 (1982).
29. J. M. Bioucas-Dias, and M. A. Figueiredo, "A new TwIST: Two-step iterative shrinkage/thresholding algorithms for image restoration," *IEEE Transactions on Image processing* **16**, 2992-3004 (2007).
30. O. Ronneberger, P. Fischer, and T. Brox, "U-net: Convolutional networks for biomedical image segmentation," in *International Conference on Medical image computing and computer-assisted intervention*(Springer2015), pp. 234-241.
31. M.-J. Sun, L.-T. Meng, M. P. Edgar, M. J. Padgett, and N. Radwell, "A Russian Dolls ordering of the Hadamard basis for compressive single-pixel imaging," *Scientific reports* **7**, 3464 (2017).
32. M. Xu, and L. V. Wang, "Photoacoustic imaging in biomedicine," *Review of scientific instruments* **77**, 041101 (2006).
33. L. V. Wang, and S. Hu, "Photoacoustic tomography: in vivo imaging from organelles to organs," *science* **335**, 1458-1462 (2012).
34. X. Wang, Y. Pang, G. Ku, X. Xie, G. Stoica, and L. V. Wang, "Noninvasive laser-induced photoacoustic tomography for structural and functional in vivo imaging of the brain," *Nature biotechnology* **21**, 803 (2003).
35. C. F. Higham, R. Murray-Smith, M. J. Padgett, and M. P. Edgar, "Deep learning for real-time single-pixel video," *Scientific reports* **8**, 2369 (2018).
36. A. Coates, A. Ng, and H. Lee, "An analysis of single-layer networks in unsupervised feature learning," in *Proceedings of the fourteenth international conference on artificial intelligence and statistics*(2011), pp. 215-223.
37. Z. Wang, A. C. Bovik, H. R. Sheikh, and E. P. Simoncelli, "Image quality assessment: from error visibility to structural similarity," *IEEE transactions on image processing* **13**, 600-612 (2004).
38. J. Limbach, C. Eisele, and G. Paunescu, "Analysis of measurement matrices for a single-pixel-camera based on both theoretical and practical performance," in *Emerging Imaging and Sensing Technologies for Security and Defence IV*(International Society for Optics and Photonics2019), p. 111630G.
39. B. E. Treeby, and B. T. Cox, "k-Wave: MATLAB toolbox for the simulation and reconstruction of photoacoustic wave fields," *Journal of biomedical optics* **15**, 021314 (2010).
40. J. R. Fienup, "Phase retrieval algorithms: a comparison," *Applied optics* **21**, 2758-2769 (1982).
41. K. Jaganathan, Y. C. Eldar, and B. Hassibi, "Phase retrieval: An overview of recent developments," *arXiv preprint arXiv:1510.07713* (2015).
42. Y. LeCun, L. Bottou, Y. Bengio, and P. Haffner, "Gradient-based learning applied to document recognition," *Proceedings of the IEEE* **86**, 2278-2324 (1998).
43. J. R. Cook, R. R. Bouchard, and S. Y. Emelianov, "Tissue-mimicking phantoms for photoacoustic and ultrasonic imaging," *Biomedical optics express* **2**, 3193-3206 (2011).